

Chapter 4

Elastic scattering measurement for ${}^7\text{Li} + {}^{159}\text{Tb}$ system

4.1 Introduction

The study of reactions that involve weakly bound nuclei shows different features in the energy dependence of the optical potential parameters, in comparison to the tightly bound nuclei (See Chapter 1). It is a well established fact that in the elastic scattering of tightly bound nuclei at energies near the Coulomb barrier, the real part shows a characteristic localized peak and imaginary part decreases as the bombarding energy decreases towards the Coulomb barrier, known as ‘Threshold Anomaly’ (TA)[6]. This may be ascribed mainly to the coupling of the elastic scattering to other reaction channels. On the contrary, the elastic scattering of weakly bound nuclei shows ‘breakup threshold anomaly (BTA)’ understood due to their low breakup threshold energies (See Sec1.4, Chapter 1). However, this observation of ‘BTA’ in some cases of target masses ranging from light to heavy mass nuclei does not hold good rather it shows absence of ‘TA’. This means no specific observation of characteristics that shows presence of ‘TA/BTA’. Thus, the study of threshold anomaly in case of weakly bound nuclei and variable target

masses remains field of great interest. There have been several works on the elastic scattering of weakly bound nuclei, both stable [9, 16, 32, 33] and radioactive beams [13, 14, 70], a systematic behavior of the energy dependence of the optical potential (OP) for such systems has not been reached. The reason may be concerned with the low intensity of radioactive ion beams and hence difficulties in the measurements as one needs very precise data in a large range of the scattering angle. At low energies where the scattering is almost entirely of Rutherford type, it is difficult to extract the interaction potential parameters from the data.

4.1.1 Present work

In the present work, very precise and complete angular distribution of the ${}^7\text{Li}+{}^{159}\text{Tb}$ system have been carried out at energies from below the Coulomb barrier ($V_{c.m.}^b=26.6$ MeV) to approximately twice this value. The total reaction cross section for this system, is also obtained and compared with systems that involve different target masses in the range from $A = 27$ to 232, to study the role of breakup (BU) on total reaction cross sections as a function of energy. In addition to the above Continuum Discretized Coupled Channels (CDCC) calculation have been carried out, to see the breakup coupling effects on elastic scattering angular distributions. The polarization potentials that have been obtained due to the breakup coupling have also been investigated and from this possible reasons for the presence of ‘TA’ have been discussed. The present experiment was carried out with ${}^7\text{Li}$ beam obtained from BARC-TIFR pelletron accelerator facility, at Tata Institute of Fundamental Research (TIFR), Mumbai, India (Fig.4.1).

4.1.2 Accelerator Facility

The BARC-TIFR pelletron accelerator facility at Tata Institute of Fundamental Research (TIFR) centre, involves two stages of acceleration to achieve higher beam energies [71]. Fig. 4.1 shows the layout of BARC-TIFR pelletron accelerator facility along with its different components. For this accelerator the maximum

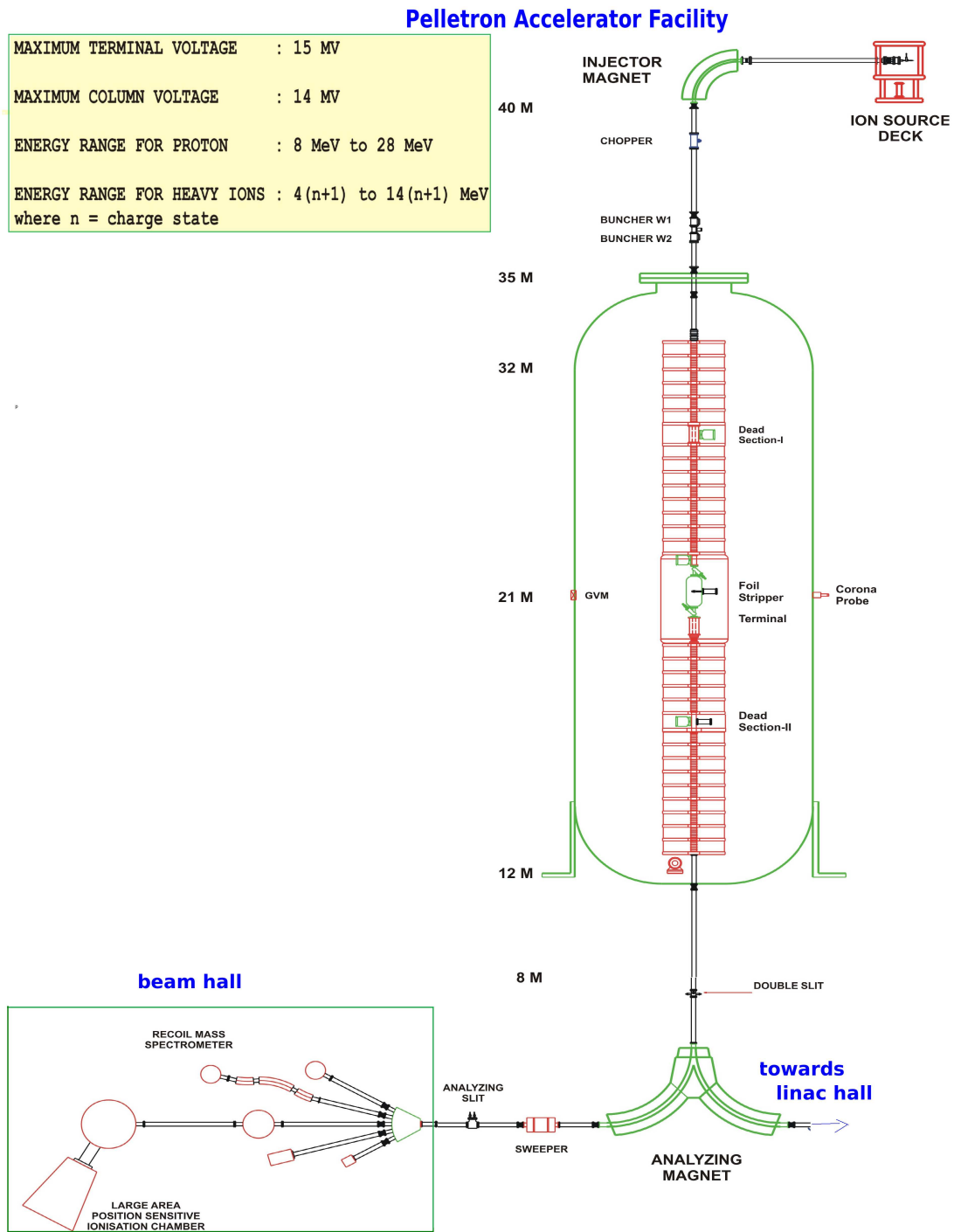


FIGURE 4.1: Schematic picture of BARC-TIFR pelletron facility at TIFR, Mumbai

terminal voltage is 14 MV. It has been named *pelletron* as it uses the chain of steel pellets for continuous transfer of charge to the terminal. This facility is capable of producing accelerated beams of nuclear particles such as protons, α -particles and different types of heavy ions at sufficient energies for investigating various nuclear phenomena in the low energy regime. Beams ranging from protons to uranium can be accelerated. In addition to continuous beams, pulsed beams of ~ 1 ns width separated by about 100 ns to 1.6 ms have also been made available by installing a double harmonic buncher in the low energy section [72].

The detail mechanism of this facility is as follows: Negative ions are generated from a SNICS (Source of Negative Ions through Cesium Sputtering) source that is situated at the top of the accelerator tower. These ions are initially accelerated to low energies (150-250 keV) in a short horizontal section. Since these negative ions may contain a mixture of many elements, a desired beam is obtained using an injector magnet that bend the beam through 90° with a suitable magnetic field and injected into the vertical accelerating column. Upon entering the vertical column, negative ions will get attracted to the positive high voltage terminal (maximum of 14 MV) that is situated at the center of the accelerating column. The high electric potential at the terminal is achieved by a continuous transfer of charge to the terminal by means of the chain of steel pellets. Thus, in the first stage, the ions will get energy V_T through the acceleration that results from the electrostatic attraction of the negative ions by the positively charged voltage terminal. Inside the terminal the ions pass through a thin carbon foil or a small volume of a gas (stripping material), where they lose electrons and acquire a high positive charge resulting in a distribution of charge states of the ion. Now, the resulting positive ions enter the second or high energy stage of acceleration where the positive ions get repelled by the positive voltage of the terminal. Hence, in the second stage of pelletron, the positive ions gain qV_T energy. In this way, at the final stage the total energy acquired by the ion will be,

$$E = V_T + qV_T \text{ MeV} \quad (4.1)$$

Where, V is the terminal voltage and q is a charge of ions.

After this stage, the ions are bent with the help of analyzing magnet to obtain the particular charge state of the ions. Here, analyzing magnet provides suitable magnetic field from the relation:

$$B = 720.76 \frac{\sqrt{AE}}{q} \text{ Gauss} \quad (4.2)$$

Where, B is the required magnetic field for the energy (E) of the analyzed ions of mass A and charge state q . In the end, after acceleration analyzed beam of ions are transported to the beam hall using five different beam lines:

- *The 0° beam line is generally used for the scattering experiment using general purpose scattering chamber (GPSC). In the present work, measurement of elastic scattering for ${}^7\text{Li} + {}^{159}\text{Tb}$ system, was carried out at this beam line.*
- *The 15° north beam line dedicated for γ -ray, neutron and charged particle spectroscopy experiments.*
- *The 30° north beam line is mainly used for irradiation of chemical and biological samples and AMS measurements.*
- *The 15° south beam line is used for recoil mass separator.*
- *The 30° south beam line is dedicated to atomic physics measurements.*

The beam transport system on these lines is remotely controlled using a CAMAC system and integrated with the indigenously developed PC based control system of the main accelerator [73].

4.2 Experimental Details

The measurements were done for the scattering of ${}^7\text{Li}$ on ${}^{159}\text{Tb}$ using 14UD Pelletron accelerator facility, Mumbai, India. The measurements were carried out at

24, 26, 28, 30, 35, 40 and 44 MeV. The ${}^7\text{Li}$ beam bombarded on self supported enriched ${}^{159}\text{Tb}$ target of thickness 1 mg/cm^2 . The beam current during the entire experiment was ranged between 20 to 40 nA. Four solid state silicon surface barrier detector telescopes were mounted on the rotating arm to detect the elastically scattered ${}^7\text{Li}$ ions. The schematic of the scattering chamber and set up was similar to the one as given in the previous chapter 3, (Fig.3.2). The detector telescopes were of thickness as follows: (i)(T_1) with $\Delta E=25\ \mu\text{m}$ and $E=300\ \mu\text{m}$. (ii)(T_2) with $\Delta E=15\ \mu\text{m}$ and $E=1.5\ \text{mm}$. (iii)(T_3) with $\Delta E=15\ \mu\text{m}$ and $E=1\ \text{mm}$. (iv)(T_4) with $\Delta E=15\ \mu\text{m}$ and $E=1\ \text{mm}$. Two monitor detectors, M_1 and M_2 were placed at 15° and 20° respectively. The telescopes were placed on a rotating arm inside a 1m scattering chamber at an angular separation of 10° between consecutive telescopes. The statistical error in the data was less than 5% in the forward angles and less than 8% in the backward angles. The electronic setup to acquire the experimental data, was same as shown in the Fig. 3.5 (See Chapter 3). The method to identify the charged particles using silicon surface barrier detectors is already given in the previous chapter (Sec.3.2.1,Chapter 3). The obtained spectrum from the present measurement is shown in the Fig.4.2, which is a typical bi parametric ΔE - E spectrum for the ${}^7\text{Li} + {}^{159}\text{Tb}$ system at $E_{lab}=40\ \text{MeV}$ and $\theta=40^\circ$. In this figure, the inset shows the corresponding projection for the $Z=3$ elastic events. The experimental data analysis was done using ‘LAMPS’ (Linux Advanced Multi parameter system) software.

4.3 Data Analysis

4.3.1 Optical Model analysis of elastic scattering angular distribution

A phenomenological Woods-Saxon Potential (WSP) was used in the optical model analysis of the elastic scattering angular distribution data using the ECIS code[60]. In the optical model analysis, the WSP has been successfully used to describe the

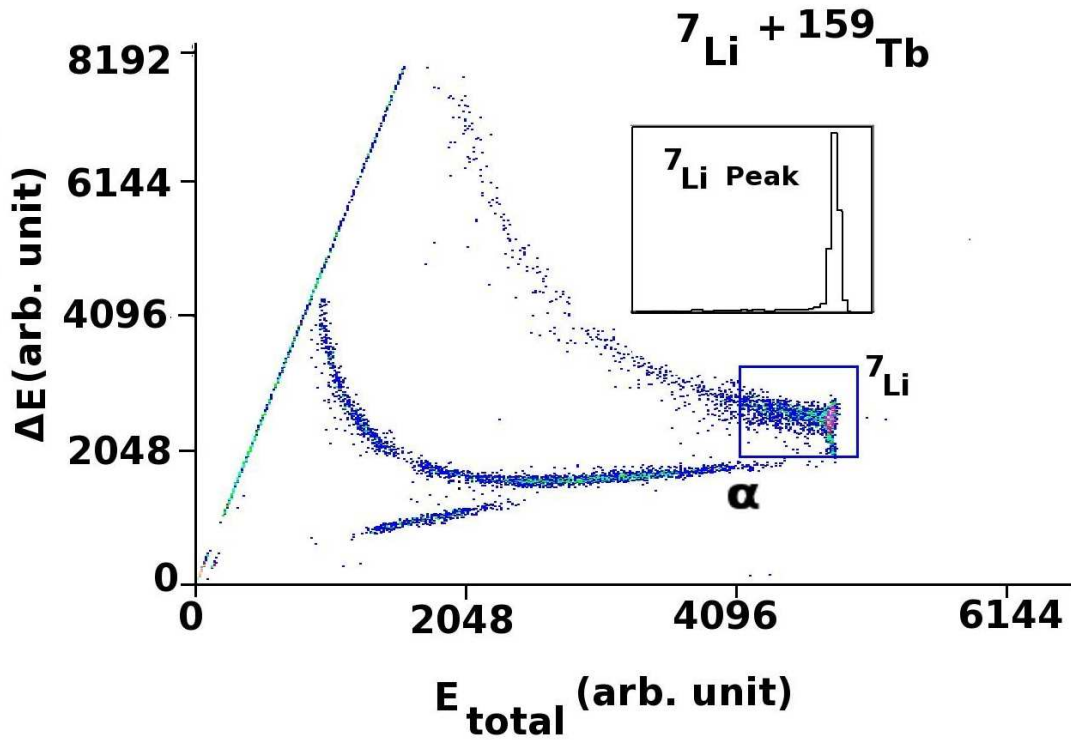


FIGURE 4.2: A typical two dimensional ΔE - E spectrum for the ${}^7\text{Li} + {}^{159}\text{Tb}$ system at $E_{lab}=40$ MeV and $\theta=40^\circ$.

large variety of systems in a wide range of energy. The real and imaginary depths of the Woods-Saxon potential have been used to get the best fit to the present data. In the optical model analysis only the depth of nuclear potentials have been varied without changing the real and imaginary diffuseness(a) and reduced radii(r_0) that were fixed at 0.63 fm and 1.2 fm, respectively. The same fit procedure was repeated with constant radii but diffuseness was varied from 0.59 to 0.67 fm, in steps of 0.02 fm. The results from of the optical model analysis using the WSP are shown in the Fig. 4.3 that gives reasonable description of the data. It was observed that several types of optical potential parameters describes the angular distributions equally well. Therefore, to reduce the ambiguities with different set of potentials, the radii of sensitivity R_{sr} and R_{si} , corresponding to the real and imaginary parts have been determined. At the radius of sensitivity different curves of potentials intersect at the same value. The point of intersection has been considered as radius of sensitivity. Fig. 4.4 shows the plot for the radii of sensitivity at one of the bombarding energy 35 MeV. The procedure to obtain the

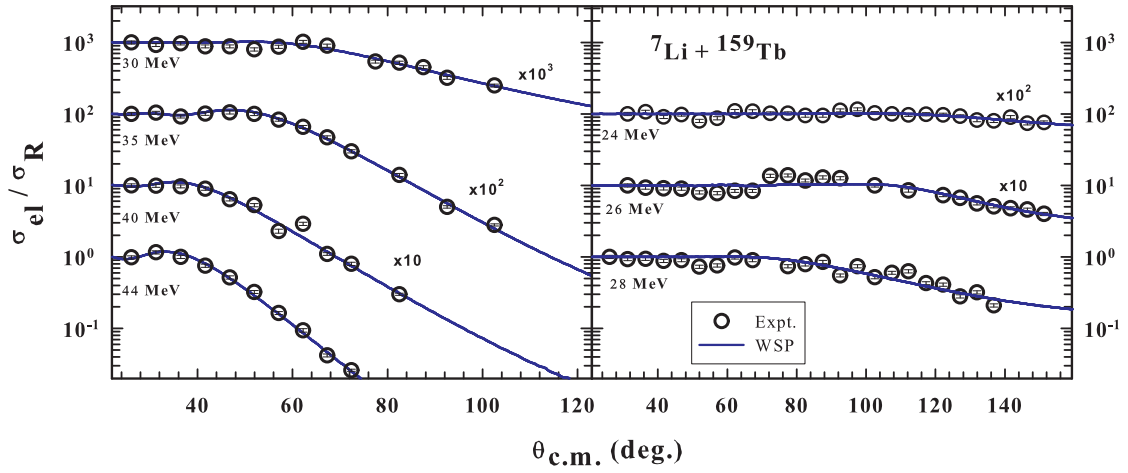


FIGURE 4.3: Experimental elastic scattering cross sections normalized to the Rutherford cross sections as a function of $\theta_{c.m.}$ for ${}^7\text{Li} + {}^{159}\text{Tb}$ system. The continuous lines represent the best fit that have been obtained from the optical model analysis using Woods-Saxon potential (WSP).

radii of sensitivity was repeated for all the other energies and average was taken for real and imaginary radii of sensitivity. Thus, at the resulted average radius (~ 11.5 fm) the potential parameters have been obtained.

The corresponding optical model potential parameters from this analysis for ${}^7\text{Li} + {}^{159}\text{Tb}$ system are given in the Table 4.1. The potential parameters have been extracted at $r \sim 11.5$ fm (the radius of sensitivity), are shown in the Fig. 4.5 for the ${}^7\text{Li} + {}^{159}\text{Tb}$ system. To calculate the error in the potential parameters, the range of deviation of the potential depths that corresponds to χ^2 variation was considered of one unit. It was observed that the real and imaginary part of the potential have roughly energy independent behavior at higher energies but at below barrier energy the imaginary part shows decreasing trend and at the same time the real part of the potential starts increasing at near barrier energy. Thus, the characteristics of the obtained real and imaginary potentials may indicate the usual ‘Threshold Anomaly’ for the ${}^7\text{Li} + {}^{159}\text{Tb}$ system. Also, the imaginary part of the optical potential almost drops to zero at the lowest energy, and the real part of the potential does not decrease in the same energy region [74].

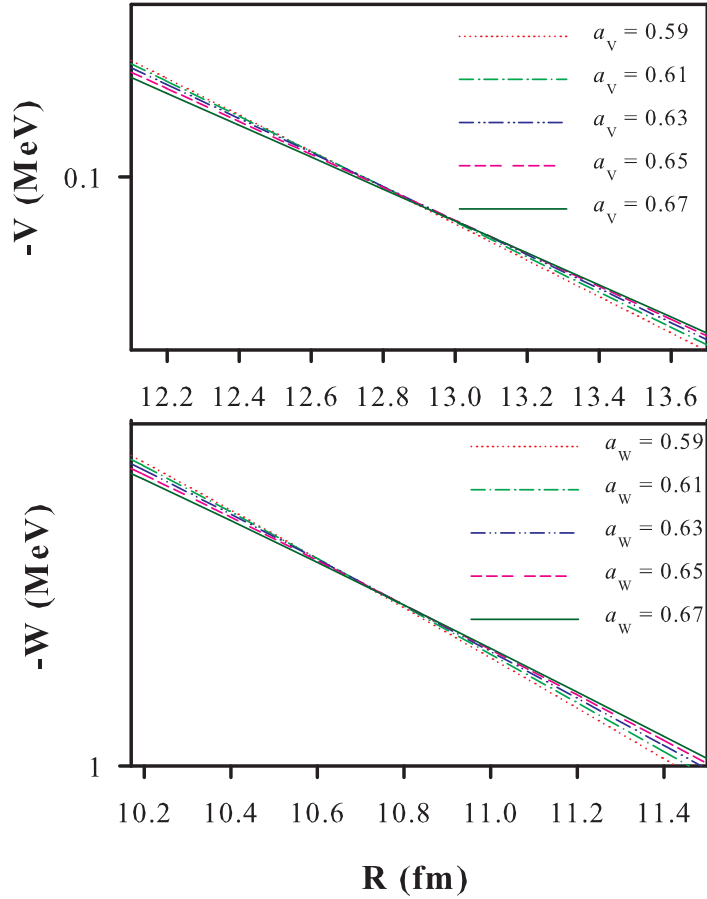


FIGURE 4.4: Plot of sensitivity radii for real (upper) and imaginary (lower) parts of the WSP potential at $E_{lab} = 35$ MeV. The real and imaginary diffuseness, a_r and a_i , have been varied in steps of 0.02 fm between 0.59 and 0.67 fm.

TABLE 4.1: Optical potential parameters and total reaction cross sections ${}^7\text{Li} + {}^{159}\text{Tb}$ system.

$E_{c.m.}$	V_o (MeV)	W_o (MeV)	χ^2_{min}/N	$\sigma_{React.}$ (mb)
22.99	66.05	7.0	2.5	51
24.90	43.44	2.15	10.0	132
26.82	1.79	81.3	13.2	566
28.73	2.44	173.80	5.3	1006
33.52	41.60	26.50	36.2	1160
38.31	52.70	72.49	8.2	1711
42.14	30.73	18.11	2.3	1579

4.3.2 Dispersion relation analysis

The method, to carry out the dispersion relation analysis is given in the chapter 2 (Sec:2.2.1). This study has been done by using the expression that relates the real and imaginary parts of the potential by,

$$V(r; E) = \frac{P}{\pi} \int_0^\infty \frac{W(r; E')}{E' - E} dE' \quad (4.3)$$

Also,

$$V(r; E) = V_o(r; E) + \Delta V(r; E) \quad (4.4)$$

Where, P is the principal value, ΔV (polarization potential) and V_o are rapidly and smoothly varying functions with respect to energy [44]. Using three different linear segments for imaginary potential the corresponding real parts were calculated from this calculation. The results for the real and imaginary parts of the potential are shown in the Figs. 4.5(a) and (b) respectively. The results show the better agreement with the observed behavior of real part of the nuclear potential.

4.3.3 Total Reaction cross sections

The total reaction cross sections from the present measurement were compared with the other systems that involve ${}^7\text{Li}$ as projectile and different target masses such as ${}^{16}\text{O}$, ${}^{27}\text{Al}$, ${}^{28}\text{Si}$, ${}^{59}\text{Co}$, ${}^{64}\text{Zn}$, ${}^{112}\text{Sn}$, ${}^{208}\text{Pb}$ and ${}^{232}\text{Th}$. If one wants to compare the reaction cross sections for different systems, it is required to suppress differences arising from the size and the charges of the systems [75]. In this reduction method, the quantities $\sigma_R / ((A_p^{1/3} + A_T^{1/3})^2)$ vs $E_{c.m.} (A_p^{1/3} + A_T^{1/3}) / Z_p Z_T$ are plotted, where, p and t are related to the projectile and the target, respectively, and σ_R is the total reaction cross section. This procedure removes the dependence on the charge and mass of the collision partners but not on specific features of the projectile density, particularly when weakly bound projectile nuclei are involved. A comparison of total reaction cross sections for the case of ${}^7\text{Li}$ -projectile and different target nuclei in the mass range from $A=16$ to 232, is represented in the

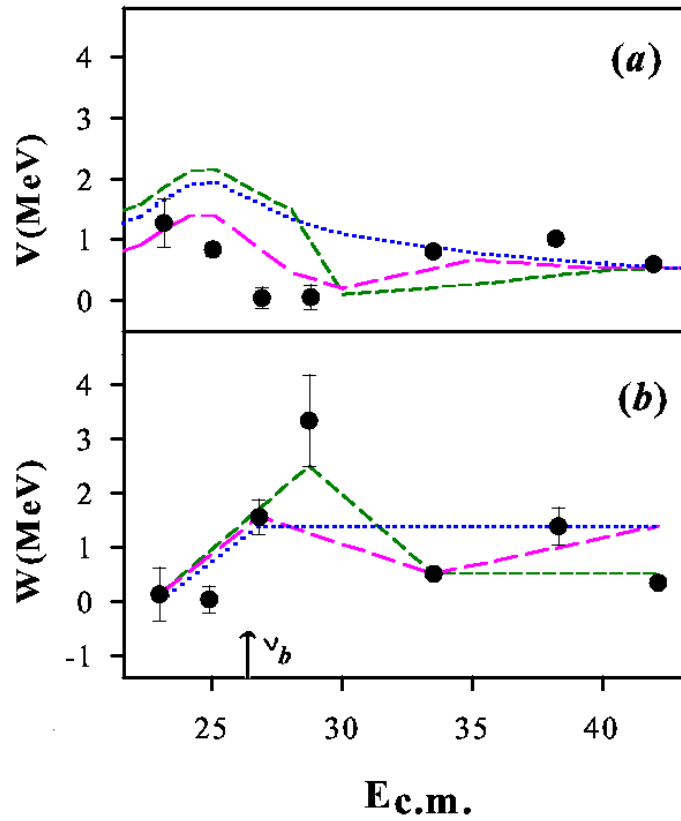


FIGURE 4.5: Energy dependence of the optical potential parameters for the ${}^7\text{Li} + {}^{159}\text{Tb}$ system at an average radius $R_s=11.5$ fm.

Fig. 4.6. At lower energies, target mass dependence of the cross sections may be observed.

4.4 Continuum Discretized Coupled-Channels (CDCC) Calculations

To investigate the projectile breakup effect on elastic scattering angular distributions, continuum discretized coupled channels calculation (CDCC) has been done using FRESKO code[42], version FRES 2.8. The details of this formalism is already given in the chapter 2 (Sec:2.6.2). In the present study, ${}^7\text{Li}$ (projectile) has been considered as $\alpha + t$ cluster and the continuum part has been discretized in small momentum bins of finite width, $\Delta k=0.20$ fm $^{-1}$ for non resonant part and

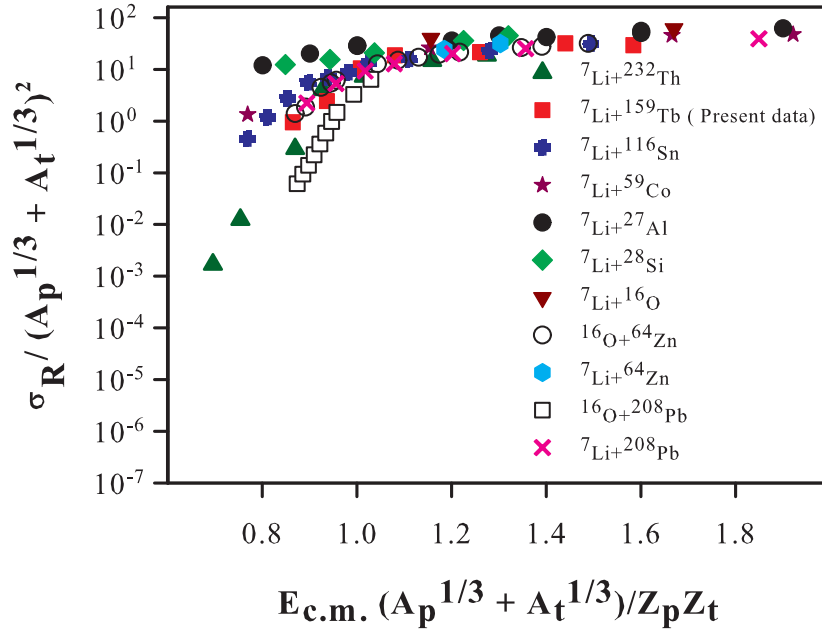


FIGURE 4.6: Reduced reaction cross sections for the systems that involve ${}^7\text{Li}$ and different target masses[20, 28, 30, 35, 76, 77, 78, 79, 80, 81]

fine binning has been done in the resonant part. In the present calculation, the bound excited state ($\frac{1}{2}^-$, 478 keV state) of ${}^7\text{Li}$ have also been incorporated. The scattering wave functions in the solution of coupled-channels calculations were integrated up to 140 fm in steps of 0.05 fm. The relative angular momentum was taken up to $110\hbar$ and the maximum excitation energy has been taken up to ~ 9 MeV. For all energy, the cluster-folded potentials were adjusted to obtain the optimum description of the elastic scattering data and fixed at ($V=113.96$ MeV, $r_o=1.2$ fm, $a_o=0.72$ fm) and ($V=123.93$ MeV, $r_o=1.245$ fm, $a_o=0.770$ fm) for $t + {}^{159}\text{Tb}$ and $\alpha + {}^{159}\text{Tb}$, respectively. The imaginary potentials were $W_o=50.0$ MeV, $r_o=1.06$ fm and $a_o=0.4$ fm. The binding potentials between the $\alpha+t$ cluster for bound and resonant states of ${}^7\text{Li}$ -projectile that calculates the bin wave functions, have been taken from the Ref.[82]. The target inelastic states were also included in the present calculation. To parameterize the nuclear deformation for the inelastic states, the transition strengths ($B(E2)$) from ($g.s., \frac{3}{2}^+$) \rightarrow (0.058 MeV, $\frac{5}{2}^+$) and (0.1375 MeV, $\frac{7}{2}^+$) that are $2.8013 \pm 0.1458 e^2 b^2$ and $1.4736 \pm 0.2047 e^2 b^2$ respectively, have been taken from the Ref.[83].

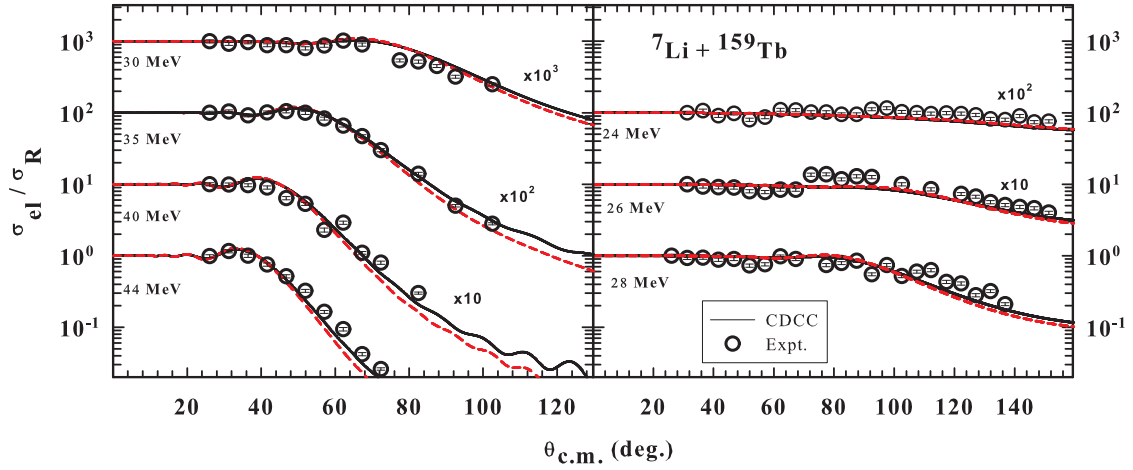


FIGURE 4.7: Experimental elastic scattering cross sections normalized to the Rutherford cross sections as a function of $\theta_{c.m.}$ for the ${}^7\text{Li} + {}^{159}\text{Tb}$ system. The results of the CDCC calculation with and without including breakup couplings are shown by continuous and dashed lines respectively.

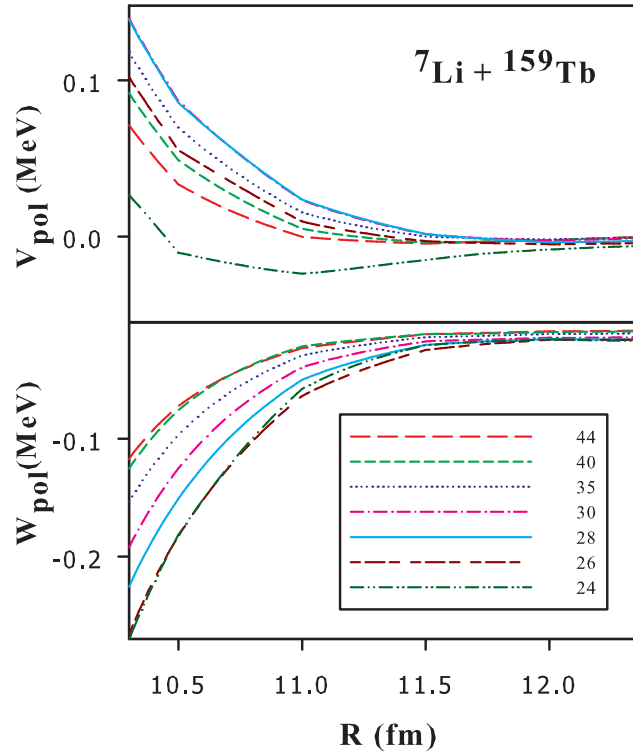


FIGURE 4.8: Real and imaginary parts of the DPP as a function of radius R at different energies for ${}^7\text{Li} + {}^{159}\text{Tb}$ system.

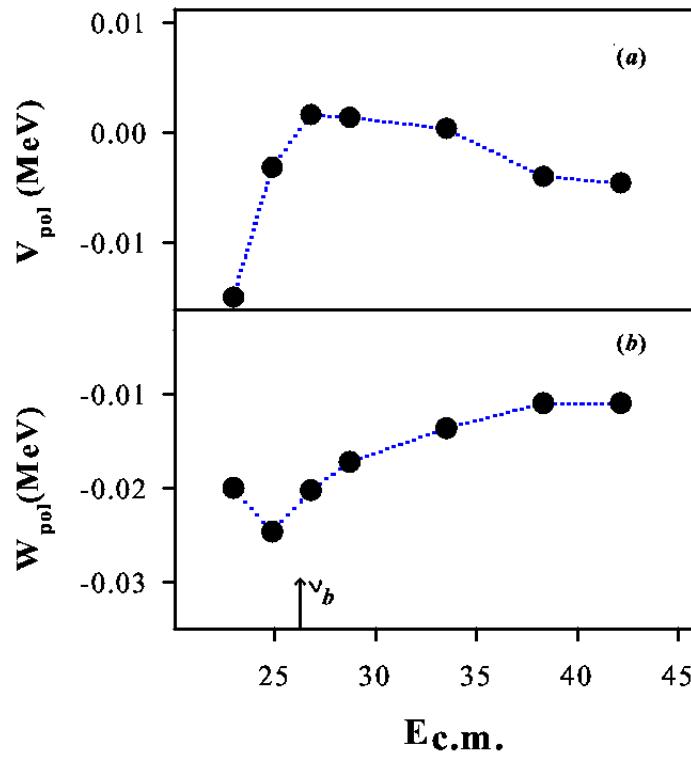


FIGURE 4.9: Real and imaginary parts of the DPP at an average radius $R_s=11.5$ fm as a function of energy for ${}^7\text{Li} + {}^{159}\text{Tb}$ system.

Fig. 4.7 shows the results of calculation with (solid line) and without (dashed line) breakup coupling. It is seen that the results of the CDCC calculations are in better agreement with the elastic scattering data. The observed effect of breakup coupling are visibly small on the elastic scattering cross section at energies above the barrier and it reduces as the barrier energy is approached.

Fig. 4.8 shows the polarization potentials as a function of R that have been derived due to the breakup coupling. As the energy increases the real part also increases and shows the repulsive nature, but as the energy approaches towards below barrier region the real part starts decreasing.

Fig. 4.9 represents the real and imaginary parts of the dynamic polarization potentials (DPP) that are obtained due to the breakup coupling at radius of sensitivity (~ 11.5 fm). One can observe that at below the barrier the imaginary potentials becomes more negative in comparison to the above barrier energy regime.

4.5 Results and Discussion

In this work, elastic scattering angular distributions have been measured at near barrier energies for ${}^7\text{Li} + {}^{159}\text{Tb}$ system. The elastic scattering data have been analyzed by Woods-Saxon Potential (WSP) using ECIS code. From the energy dependence of the potential parameters, it can be seen that the imaginary potential shows decreasing trend at very near barrier energy while at the same time the real part of the potential starts increasing in the same energy region. The observed behavior of real and imaginary parts of the potential may indicate the presence of the ‘Threshold Anomaly’. From the dispersion relation analysis, the real and imaginary parts of the potentials are observed to be consistent with the observed behavior of the OM potentials. To understand the projectile breakup effect on the elastic scattering angular distributions, continuum discretized coupled channels calculations have been carried out. The net effect of the real and imaginary parts of the dynamic polarization potential (DPP) seems attractive in nature that reduces the barrier and may be responsible for the enhancement in the fusion cross sections. The behavior of DPP with respect to the radius R as well as energy favors the indication of ‘Threshold Anomaly’. This may also be due to the net polarization potential, composed by competing attractive and repulsive parts, depends strongly on the bound state of ${}^7\text{Li}$ -projectile and also depends on target inelastic contributions. From the systematic study of total reaction cross sections for ${}^7\text{Li}$ -projectile and variety of target nuclei in the mass range from $A=16$ to 232, it can be observed that the total reaction cross sections have little target mass dependence at lower energies.